

## MATERIALS SCIENCE

# Growth rules for irregular architected materials with programmable properties

Ke Liu<sup>1,2</sup>, Rachel Sun<sup>1†</sup>, Chiara Daraio<sup>1\*</sup>

Biomaterials display microstructures that are geometrically irregular and functionally efficient. Understanding the role of irregularity in determining material properties offers a new path to engineer materials with superior functionalities, such as imperfection insensitivity, enhanced impact absorption, and stress redirection. We uncover fundamental, probabilistic structure–property relationships using a growth-inspired program that evokes the formation of stochastic architectures in natural systems. This virtual growth program imposes a set of local rules on a limited number of basic elements. It generates materials that exhibit a large variation in functional properties starting from very limited initial resources, which echoes the diversity of biological systems. We identify basic rules to control mechanical properties by independently varying the microstructure's topology and geometry in a general, graph-based representation of irregular materials.

The properties of materials depend both on their chemical composition and on the geometry of their microstructures. Empowered by carefully engineered sub-scale microstructures, architected materials (1–5) have been suggested for applications in optics (6), electromagnetics (7, 8), acoustics (9), and robotics (10–12). In mechanics (13), architected materials have been designed to exhibit negative thermal expansion (14), negative Poisson's ratio (15), ultrahigh strength-to-weight ratio (16, 17), tunable failure load (18), vanishing shear modulus (19), and shear-normal coupling (20). To reduce the complexity of designing structures in a nearly infinite space, human-made architected materials are mostly designed by periodic tessellations of selected geometric motifs. These motifs are either derived empirically from a limited number of known geometries, such as biomaterials, crystalline solids, and art (15, 16, 21), or computationally generated within bounding boxes discretized into pixels or voxels (22–25).

Materials with periodic microstructures are special cases in the realm of architected materials. Natural materials are usually characterized by irregular and heterogeneous microstructures, such as wood (26), nacre (27), insect nests (28) (Fig. 1A), or human bones (29). They present distinctive properties, such as the exceptionally white scales of some beetles (30) or the functional stability to perturbations of proteins (31). The geometric irregularity of biomaterials is a natural outcome of self-organized growth, which unfolds through a distributed, stochastic building process that follows simple local rules without a centralized plan (28).

Understanding the independent role of geometry and topology in irregular microstructures provides opportunities for the design and fabrication of advanced engineering materials. However, current descriptions of geometry used for periodic systems lead to ambiguity in distinguishing the contribution of specific structural features, or their repetition, on given functionalities. This underlines the importance of developing tools to define spatial characteristics in irregular materials.

Recently, computational methods have been developed to design and characterize irregular microstructures (32–36). For instance, the design of random, auxetic truss lattices revealed important connections between Poisson's ratio and lattice connectivity (33, 34). However, these tools do not provide a general framework to describe the geometry of architected materials, for example, because they do not include periodic designs in their descriptors.

## A virtual growth program for microstructure generation

To better understand the structure–property relationships in irregular architected materials, we created a tool that evokes the distributed stochastic building process of natural growth, which we call the virtual growth program. The program is a graph-based method that builds on the combinatorial space of basic building blocks (Fig. 1B). These building blocks are local structural elements that can be identified in arbitrarily complex microstructures at a scale that is smaller than the typical unit cells in periodic designs. In the virtual growth process, the building blocks are connected stochastically on an underlying network, in which each pair of neighbors abides prescribed adjacency rules (Fig. 1, C and D). In this framework, a material's microstructure can be both periodic and nonperiodic. The framework also decouples topology (the connectivity of the underlying network) from the geometry (the shape of the

building blocks) and allows investigating their independent influence on global material properties.

In this work, we use the virtual growth process to unravel structure–property relationships in irregular architected materials. We show that by starting from a very limited number of local structures (i.e., the building blocks), it is possible to generate a rich set of material microstructures with a wide range of functional properties. Specific properties can be targeted, by selecting adjacency rules and building blocks availability during “growth.” These findings provide insight into how to program material properties in stochastic, self-assembly processes, and may influence future manufacturing of engineering materials.

The virtual growth program relies on four major inputs, which serve as the genome for the generation of architected materials: (i) the topology of the underlying network, (ii) the geometry of building blocks, (iii) the adjacency rules between building blocks, and (iv) the availability of (or frequency hint for) building blocks. The program can create materials with different microstructures (Fig. 2). For example, the same square network (Fig. 2A) can be used to accommodate different building blocks (Fig. 2, B to D), including their reflections and rotations (fig. S1A). The adjacency rules define whether and how the basic building blocks can pair with each other (fig. S1B) by enforcing geometrical compatibility at the interface and avoiding unwanted geometric features. For example, in the case of Fig. 2B, we forbid two “L”-shaped building blocks from connecting to avoid forming disconnected loops. The availability of building blocks resembles natural resource limits and influences how many times each building block appears in the final design (fig. S1C). Infinite availability of building blocks leads to constant frequency hints throughout the “growth” process. Defects are likely to happen when the availability of a certain building block is very low (fig. S1, D and E). To avoid defects, in the rest of this study, we assume that there is an infinite amount of building blocks available for each “growth” process.

The virtual growth process (movie S1) implements a *WaveFunctionCollapse* algorithm (37). In each step, the algorithm assigns a random building block to the node on a predefined network with minimal nodal entropy. Here, nodal entropy is related to the number of building blocks that can be assigned to a given node. For example, if only one building block can be assigned to a given node to satisfy adjacency rules, then its nodal entropy is zero. If a node can be filled with any building block, its nodal entropy is maximal. When the algorithm cannot assign any building block to a node, a defect forms. This process continues until all nodes are assigned, and the nodal entropies are updated after each step.

<sup>1</sup>Department of Mechanical and Civil Engineering, California Institute of Technology, Pasadena, CA 91125, USA.

<sup>2</sup>Department of Advanced Manufacturing and Robotics, Peking University, Beijing 100871, China.

\*Corresponding author. Email: [daraio@caltech.edu](mailto:daraio@caltech.edu).

†Present address: Department of Mechanical Engineering, Massachusetts Institute of Technology, Cambridge, MA 02139, USA.

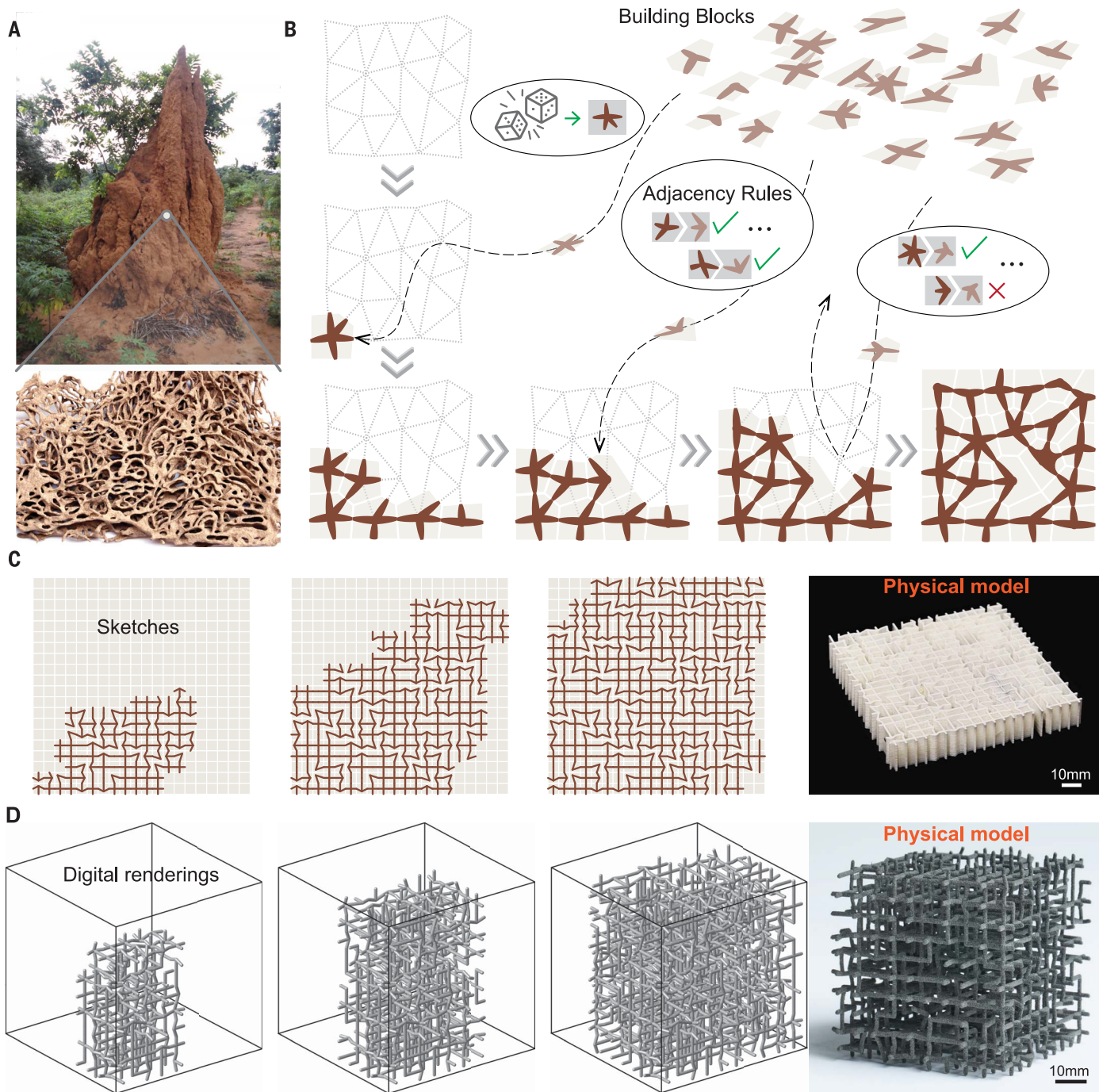


**Fig. 1. Schematic of the virtual growth process of irregular architected materials.** (A) Termite nests have irregular internal structures that are optimized for structural stability and ventilation (28). (B) Abstraction of the “growth” process, which assigns building blocks on an underlying graph. (C and D) Illustration of the virtual growth process (C) in 2D (movie S1) and (D) in 3D (movie S2). The physical models in (C) and (D) are 3D printed.

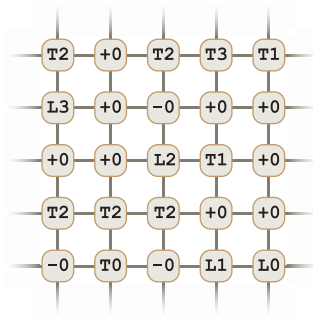
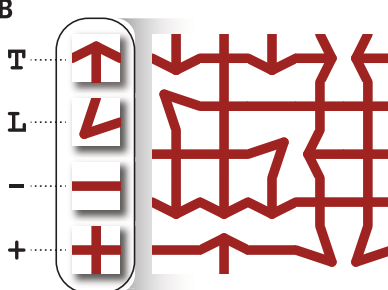
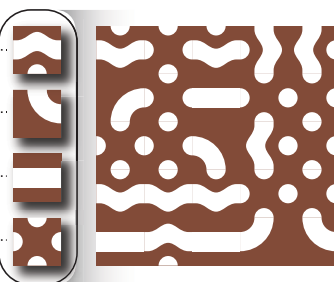
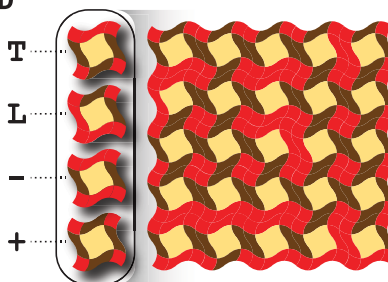
Downloaded from https://www.science.org at Peking University on August 25, 2022

**Clustering and convergence of material properties**  
We constrain the underlying network to be a squared grid, without loss of generality, and use the building blocks in Fig. 2B and fig. S1. The nondeterministic assignment of building blocks leads to a diversity of architected materials. Even given the same building blocks, adjacency rules, and frequency hints, the program generates different material microstructures every time. After generating the microstruc-

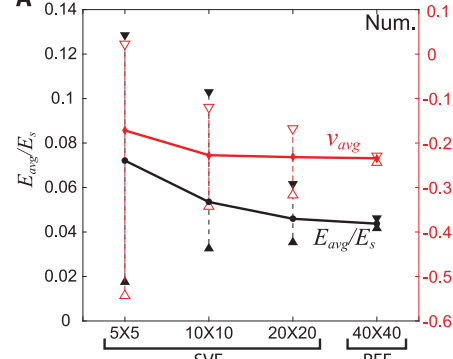
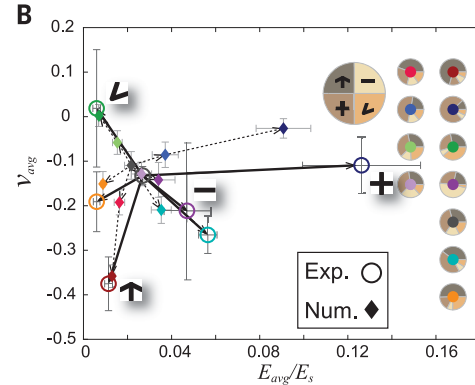
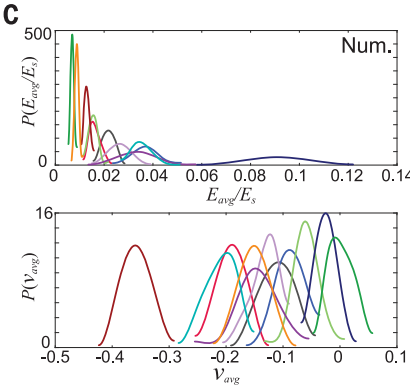
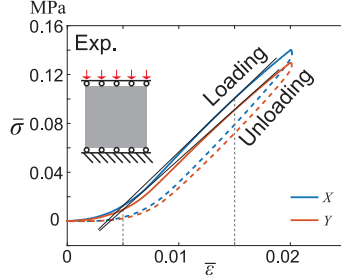
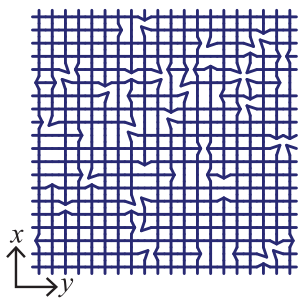
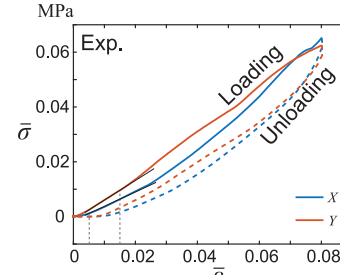
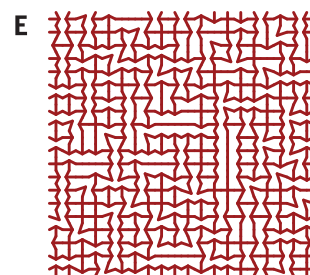
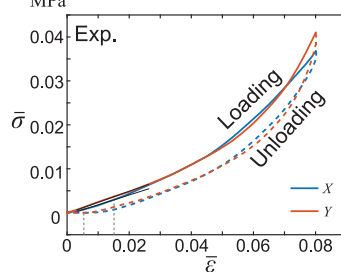
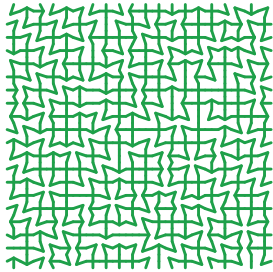
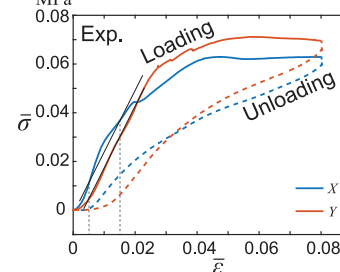
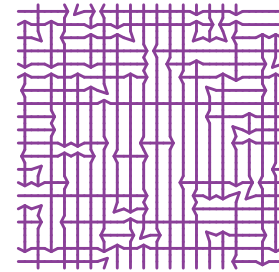
tures, we evaluate their linear elastic properties, Young’s modulus, and Poisson’s ratio in the  $x$  and  $y$  directions. To obtain these properties, we perform numerical homogenization (38) using the statistical volume element (SVE) approach (39). The convergence of linear elastic properties is tested on three different sample sizes for the SVE and compared to the results of direct simulations on larger patches (40 by 40 squared grid) of materials. As observed

in Fig. 3A, when the SVEs are of grid size 20 by 20, their properties are close enough to that of the large 40 by 40 samples. Therefore, for each particular set of inputs to the virtual growth program, we generate 100 material samples on a grid with 20 by 20 nodes and obtain the distribution of mechanical properties by evaluating these 100 samples.

We evaluate 11 groups of architected materials generated by different frequency hints,

**A****B****C****D**

**Fig. 2. Irregular materials generated by the virtual growth program.** (A) Typical output of the virtual growth program, which is a symbolic graph. The letters and numbers are indexes that refer to the basic building blocks and their orientations. (B) Lattice-like design, which is the focus of this article. The “-,” “T,” “L,” and “+” symbols represent the building blocks in the box. (C) Spinodal pattern-like design. (D) Multimaterial composite. We note that the building blocks are not limited to square shapes as long as the interfaces between building blocks are compatible.

**A****B****C****D****E****F****G**

**Fig. 3. Mechanical properties of the 2D irregular architected materials.** (A) Numerically evaluated Young's modulus ( $E_{avg}/E_s$ ) and average Poisson's

ratio ( $\nu_{avg}$ ) values for different sizes of materials samples as a function of the dimension of the underlying networks. The first three groups are evaluated by

homogenization (SVE), and each point with error bars contains 100 samples. The (last) reference group contains 10 samples and is evaluated by a direct simulation, with boundary condition as shown in the inset of (D). The error bars extend minimal and maximal values. Num, numerical; Ref, reference. (B) Plot of  $E_{\text{avg}}/E_s$  vs.  $v_{\text{avg}}$  for 11 sample groups generated by using different frequency hints, each containing numerical 100 samples. The insets use pie plots to show the resultant probabilities of appearance of the basic building blocks. Experiments are performed for seven groups, each with five samples. The error bars extend to one standard deviation. The arrows indicate trends of property changes. Exp,

experimental. (C) Smoothed distributions of  $v_{\text{avg}}$  and  $E_{\text{avg}}/E_s$ , based on the numerical samples. The color code follows (B).  $P$ , probability density function. (D to G) Representative designs and their experimental stress ( $-\sigma$ )-strain ( $-\varepsilon$ ) curves under compression along both  $x$  and  $y$  directions (movie S3). The stresses ( $-\sigma$ ) are calculated as effective stress for the bulk volume, in units of megapascals. The stress and strains are effective values with respect to the bulk dimension of architected materials. The colors of the designs refer to the different sample groups. The inset shows the boundary conditions. The thin black lines show our definition of Young's modulus as a secant modulus between 0.005 and 0.015 strain.

but with the same basic building blocks and adjacency rules (Fig. 3B). The experimental samples are manufactured by three-dimensional (3D) printing that uses a stiff rubbery material [Semiflex, NinjaTek (38)]. In the examples shown in Fig. 3B, the generated materials exhibit nearly tetragonal symmetry (not isotropic) with similar effective Young's moduli and Poisson's ratio when loaded along the  $x$  and  $y$  directions (38). Hence, we use their average values, i.e.,  $E_{\text{avg}}$  (average effective Young's modulus) and  $v_{\text{avg}}$  (average Poisson's ratio), to compare performance of different architected

materials' groups. To obtain a dimensionless measurement,  $E_{\text{avg}}$  is normalized by the Young's modulus of the constituent material ( $E_s$ ). From the numerical samples (fig. S2), irregular architected materials of the same group tend to cluster together, in different patterns. The marginal distributions of  $E_{\text{avg}}$  and  $v_{\text{avg}}$  are shown in Fig. 3C. The experimental samples also follow similar trends in properties' distribution, in agreement with numerical simulations.

To study the structure–property relation determined by the presence of different building blocks, we focus on analyzing the mean values

of the clusters (Fig. 3B). We observe that the probabilities of appearance of different building blocks have a distinctive impact on the mechanical properties. For example, a higher probability of the "T"-shaped building block yields a decreasing Poisson's ratio toward negative values but has minimal influence on the material's average Young's modulus. A higher probability of "+"-shaped building block yields a larger Young's modulus, but it has negligible effects on the Poisson's ratio. In addition, a higher probability of both "T"- and "+"-shaped building blocks leads to materials with a

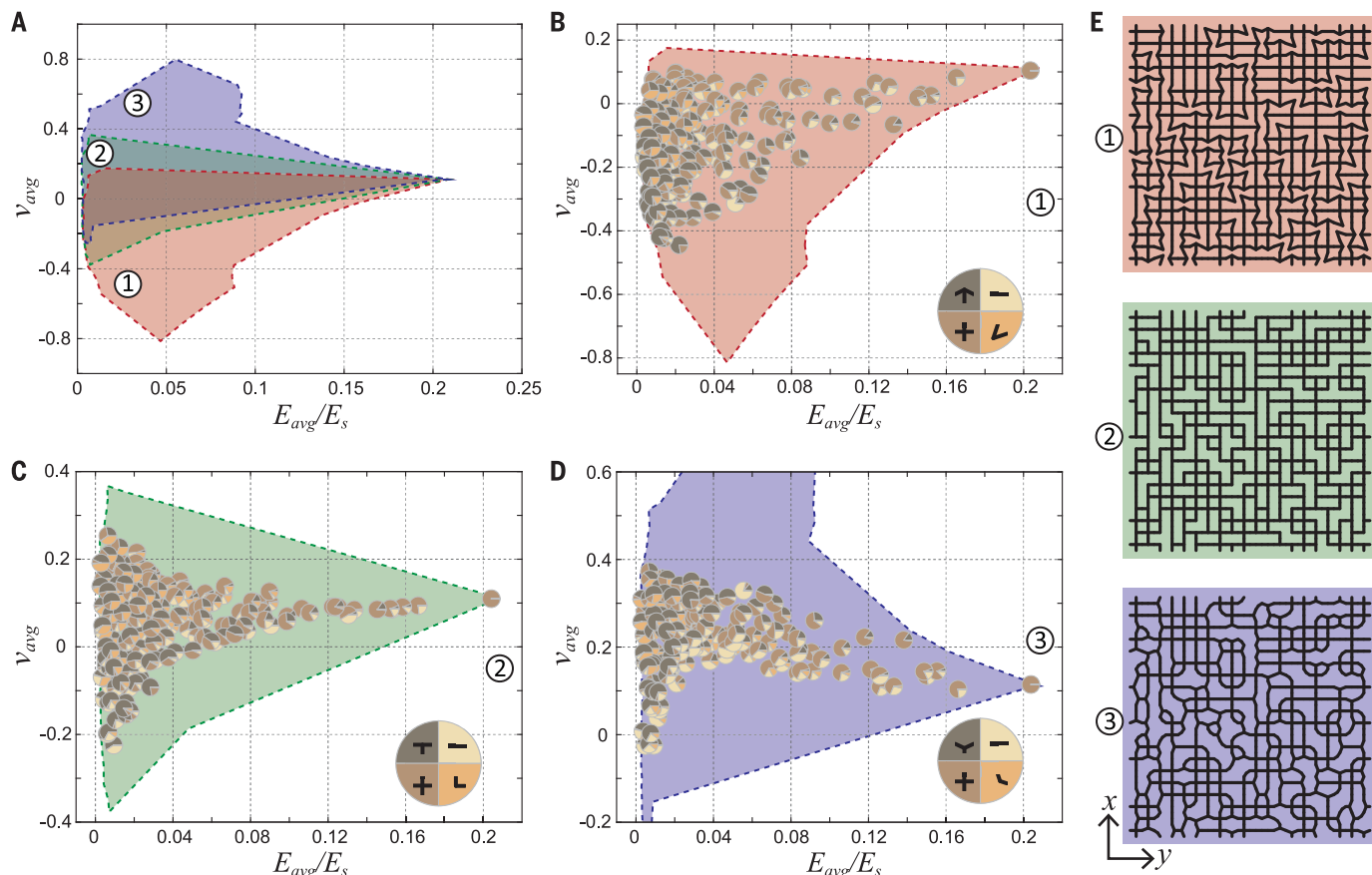


**Fig. 4. Decoupled effect of topology and geometry on material properties.**

(A) Ranges of properties covered by three different databases of samples, each obtained with different variants of building blocks. The dashed boundary of each cloud reaches to the extremal values of individual samples. (B to D) Zoom-in distribution of samples in each database. The pie plots are located at the mean

value of a group of 100 samples, with fractions of the pie showing probabilities of appearance of the corresponding building blocks. The insets show the geometries of the basic building blocks and their reference colors in the pie plots. (E) Typical designs from each of the three databases are shown, with the background colors matching the colors of the corresponding database.

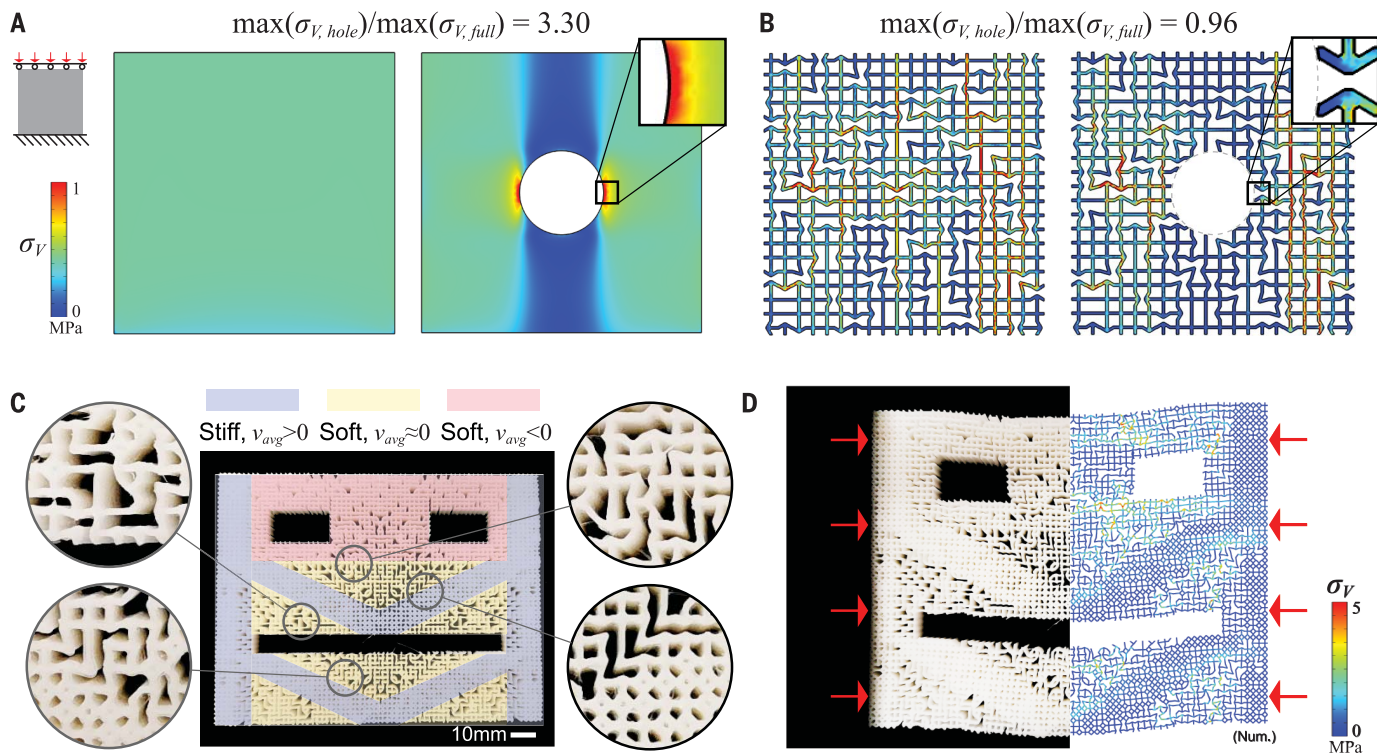


**Fig. 5. Redirection of stresses and deformations.** (A and B) Stress distribution in a piece of material compressed by a prescribed displacement, with and without the presence of a hole. (A) Piece of continuum material that has the same elastic properties as the homogenized properties of the irregular sample in (B). (B) Piece of irregular architected material. For all four cases in (A) and (B), the boundary condition and the color scale of Von Mises stress ( $\sigma_V$ ) are shown on the left. Insets show a zoom-in view of stress near the hole.

(C and D) Face that “smiles” under lateral compression, owing to its heterogeneous microstructures. (C) 3D printed structure before compression. The false color shades refer to regions generated by different frequency hints that lead to different mechanical properties. The zoomed-in views show the smooth transition between different regions of the microstructure. (D) Structure during compression. The right half shows the stress distribution from numerical simulation. The arrows show the direction of loading.

relatively high Young's modulus and relatively large negative Poisson's ratio, displaying an additive influence of building block probabilities on mechanical properties. Such trends are robust and remain consistent in both numerical and experimental results. We note that the resultant probabilities of appearance of the building blocks in the generated material samples are slightly different from the input frequency hints. This is due to the constraints imposed by the adjacency rules, as compatibility requirements override the frequency hints (fig. S3).

We observe some hysteresis effects from the experimental stress-strain curves (Fig. 3, D to G). This is likely due to the constituent material's viscoelasticity and large deformation-induced contacts and frictions between nearby elements (fig. S4). Nevertheless, we only focus on the linear regime of the experimental loading curves and extract the value of the Young's modulus in a particular direction, as the secant modulus between 0.005 and 0.015 strain. We use a digital image correlation system to track the deformations and obtain the values of Poisson's ratio (38). The discrepancies between the numerical and experimental results (Fig. 3B) are possibly caused by imperfect

boundary conditions (e.g., friction), manufacturing error, and local nonlinear effects. In particular, the group of samples with a high probability of the “—” building block (Fig. 3G) experiences strong nonlinear effects, as the long beams buckle immediately after being loaded. In fact, our experiments show that not only the linear elastic properties but also the nonlinear responses of the samples from the same group tend to behave similarly (fig. S3).

#### Construction of material databases

The virtual growth program efficiently generates materials that cover a wide range of linear elastic properties (Fig. 3). Hence, it can be used as a tool to explore the design and property space of architected materials by varying inputs. We demonstrate how changing both the topology and geometry of material microstructures (Fig. 4) results in three databases that contain 54,000 samples of architected materials.

The three clouds in different colors refer to the material samples that were generated by using three geometric variants of the building blocks. Each cloud consists of 180 groups of samples generated by 180 different combina-

tions of frequency hints (38). The angles of the “T”-shaped and “L”-shaped building blocks are changed from an acute angle to a right angle and to an obtuse angle (Fig. 4, B to D). The red shaded cloud is occupied by the material samples that were generated by using the first set of variants. Because these materials are rich in the “T”-shaped building blocks with a re-entrant acute angle, they mostly appear to be auxetic. As we change the geometries of the building blocks (Fig. 4, C and D), the range of the average Young's modulus remains almost the same, but the Poisson's ratio of the entire cloud shifts toward the positive range (Fig. 4A). An obvious negative correlation is observed between the average Poisson's ratio and the probability of the appearance of the “T”-shaped building block (fig. S5). In general, the growth rules and mechanical properties present nontrivial yet clear correlations (fig. S5). Typical materials from each of the three clouds of samples are shown in Fig. 4E. Despite the different geometries, these three samples share the same topology because they have the same underlying network, only filled with different building blocks, similar to the examples in Fig. 2.

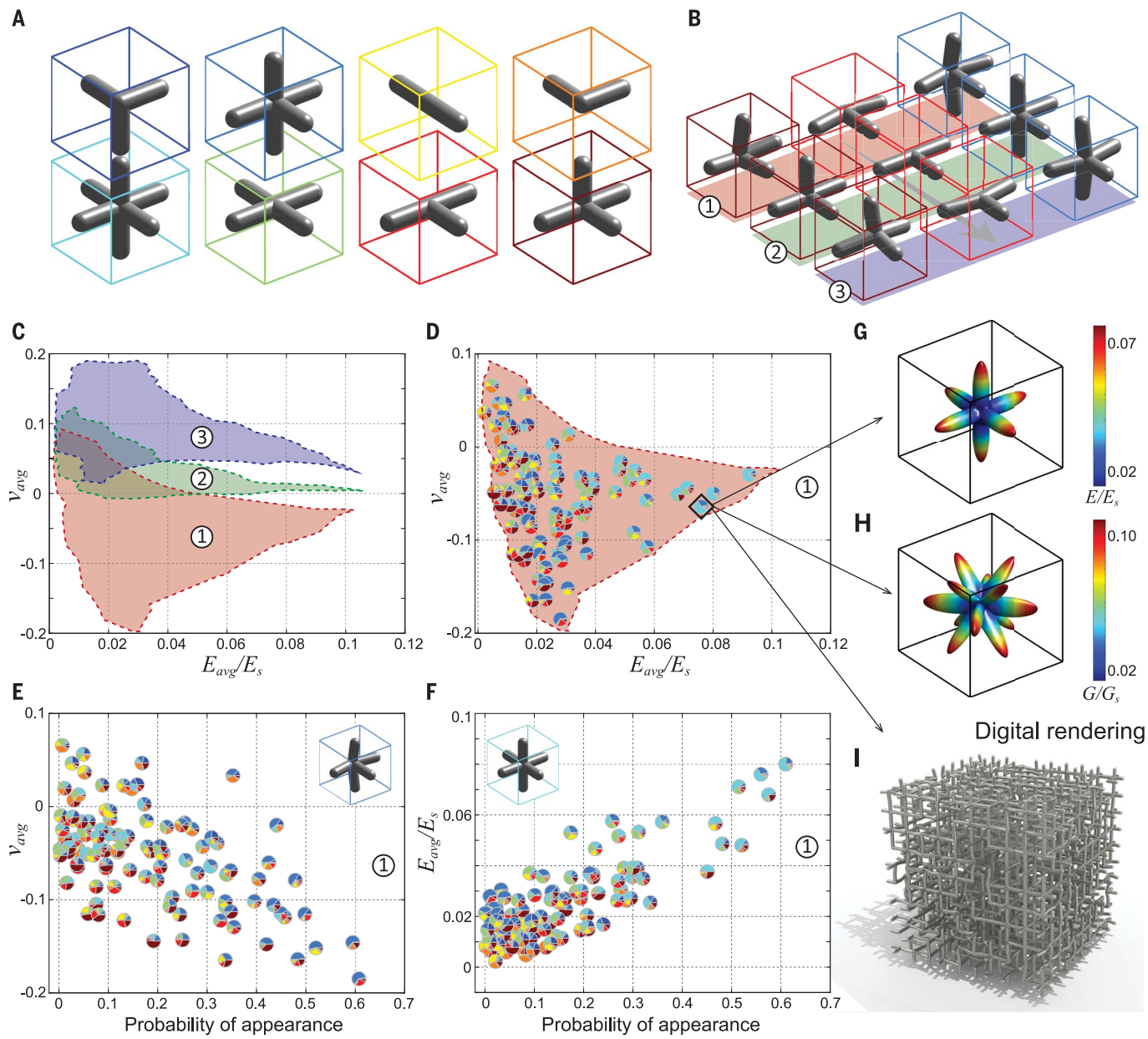


**Fig. 6. Extension to 3D irregular microstructures.** (A) Basic building blocks. (B) Three geometric variants of selected building blocks. (C) Ranges of properties covered by the generated architected materials. Each cloud corresponds to the database that was generated by using different variants of building blocks in (B). (D) Zoom-in distribution of samples in the first database. The pie plots are located at the mean value of a group of 100 samples, with fractions of the pie showing probabilities of appearance of the building blocks

within the bounding box of the corresponding color in (A). (E and F) Influence of the probability of appearance of certain basic building blocks (insets) on different mechanical properties. (G and H) Directional Young's modulus ( $E$ , normalized by  $E_s$ , the Young's modulus of the constituent material) and shear modulus ( $G$ , normalized by  $G_s$ , the shear modulus of the constituent material) of the group of samples marked a diamond box in (D). (I) Digital rendering of a material sample in the marked group in (D).

With the virtual growth program, we can obtain a wide range of irregular, yet programmable, architected materials. The programmable properties result from the nontrivial probability distribution of the stochastic topologies and geometries. The property space can be further expanded. For example, we can introduce directional preferences of the building blocks, which drives the current nearly tetragonal elasticity to orthotropic. Moreover,

by adding new building blocks, we can substantially improve the overall shear modulus of the generated materials [see (38) and fig. S6 for elaboration].

One advantage offered by irregular materials is that they offer redundant load paths: When one part of the material is damaged, the stress within the irregular architecture is redistributed through the complex microstructural network. This redistribution ensures

that the maximum stress anywhere within material remains almost the same, before and after damage, which prevents a cascading failure. We compare the stress distribution in a continuum and in an irregular architected material, before and after punching a hole in the sample (Fig. 5, A and B). Results of compression tests show that, although the uniform sample shows classical stress concentration near the hole, the irregular material shows no

such stress concentration. Rather, the stress in the sample with a hole is redistributed throughout the entire sample without drastic variations in peak stress, compared with peak stress values of the sample without a hole.

Irregular microstructures can be designed to present heterogeneous distributions of local elastic properties (40). For nonperiodic architected materials that are designed from a database of unit cells (24), tessellating different structures and constituent materials while ensuring connectedness and compatibility is challenging (25, 40, 41). By using the virtual growth program, designing materials with inhomogeneous properties is possible with a single, continuous process by assigning different frequency hints to different regions of the sample. With this approach, connectedness and compatibility are automatically guaranteed by the adjacency rules. For instance, we show how it is possible to design an inhomogeneous microstructure that can concentrate deformations in selected areas of a sample. We highlight this ability by designing a “face” that “smiles” when being compressed from the sides (Fig. 5, C and D). To change the deformation characteristics, we assigned different frequency hints to the different regions on the “face” (Fig. 5C). These sets of frequency hints are extracted from our databases (Fig. 4 and fig. S6).

By defining 3D building blocks (Fig. 6A) and adjacency rules, the virtual growth program can be extended to produce 3D irregular architected materials. Similar to the 2D case, we constructed a database of 33,000 material samples that were based on three different geometric variations on selected building blocks (Fig. 6B) and 110 different frequency hints (Fig. 6, C and D). Each material sample is generated on a 10 by 10 by 10 cubic grid. Each building block is enclosed in a cube of size 5 mm by 5 mm by 5 mm, and the lattice (beam) members are assumed to be circular, with a radius of 1 mm. We observe interesting correlations between the probabilities of appearance of building blocks and the mechanical properties (Fig. 6, E and F, and figs. S7 to S9). The anisotropy of the generated materials can be seen from the directional Young's modulus and shear modulus (Fig. 6, G and H) as a result of our particular selection of basic building blocks. A rendered image of a typical sample highlights the 3D irregular architecture (Fig. 6I).

## Discussion and outlook

We describe fundamental, probabilistic rules that control the overall mechanical response of irregular materials. Our approach establishes a general, graph-based representation of material microstructures, which we use to create architected materials with functionally graded properties and to demonstrate robustness against damage. In the future, the approach could be further extended to design materials with prespecified properties by incorporating optimization approaches in the selection of building blocks and/or in the adjacency rules for growth. The basic building blocks could also be selected to have more geometries (e.g., learned from data), different constitutive materials, and dimensional scales (e.g., to realize hierarchical materials). The underlying graph, which in this work is represented as squared or cubic grids, can be extended to have more complex connectivity. Because the virtual growth program is independent from any particular material properties, it is readily applicable to discover nonlinear and multiphysical properties of materials.

## REFERENCES AND NOTES

- K. Bertoldi, V. Vitelli, J. Christensen, M. van Hecke, *Nat. Rev. Mater.* **2**, 17066 (2017).
- H. Nassar et al., *Nat. Rev. Mater.* **5**, 667–685 (2020).
- L. Wu et al., *Mater. Today* **44**, 168–193 (2021).
- N. A. Fleck, V. S. Deshpande, M. F. Ashby, *Proc. R. Soc. A Math. Phys. Eng. Sci.* **466**, 2495–2516 (2010).
- L. A. Shaw et al., *Nat. Commun.* **10**, 291 (2019).
- Z. Vétesy et al., *J. Microsc.* **224**, 108–110 (2006).
- D. Schurig et al., *Science* **314**, 977–980 (2006).
- W. Man et al., *Proc. Natl. Acad. Sci. U.S.A.* **110**, 15886–15891 (2013).
- M. I. Hussein, M. J. Leamy, M. Ruzzene, *Appl. Mech. Rev.* **66**, 040802 (2014).
- J. I. Lipton et al., *Science* **360**, 632–635 (2018).
- C. Luo et al., *Mater. Horiz.* **7**, 229–235 (2020).
- M. Skouras, B. Thomaszewski, S. Coros, B. Bickel, M. Gross, *ACM Trans. Graph.* **32**, 1–10 (2013).
- G. W. Milton, A. V. Cherkaev, *J. Eng. Mater. Technol.* **117**, 483–493 (1995).
- Q. Wang et al., *Phys. Rev. Lett.* **117**, 175901 (2016).
- P. P. Pratapa, K. Liu, G. H. Paulino, *Phys. Rev. Lett.* **122**, 155501 (2019).
- L. R. Meza, S. Das, J. R. Greer, *Science* **345**, 1322–1326 (2014).
- X. Zhang, A. Vyatskikh, H. Gao, J. R. Greer, X. Li, *Proc. Natl. Acad. Sci. U.S.A.* **116**, 6665–6672 (2019).
- S. S. Injeti, C. Daraio, K. Bhattacharya, *Proc. Natl. Acad. Sci. U.S.A.* **116**, 23960–23965 (2019).
- M. Kadic, T. Bückmann, N. Stenger, M. Thiel, M. Wegener, *Appl. Phys. Lett.* **100**, 191901 (2012).
- T. Frenzel, M. Kadic, M. Wegener, *Science* **358**, 1072–1074 (2017).
- D. Yang et al., *Extreme Mech. Lett.* **6**, 1–9 (2016).
- Y. Mao, Q. He, X. Zhao, *Sci. Adv.* **6**, eaaz4169 (2020).
- D. Chen, M. Skouras, B. Zhu, W. Matusik, *Sci. Adv.* **4**, eaao7005 (2018).
- C. Schumacher et al., *ACM Trans. Graph.* **34**, 1–13 (2015).
- E. D. Sanders, A. Pereira, G. H. Paulino, *Sci. Adv.* **7**, eabf4838 (2021).
- J. Song et al., *Nature* **554**, 224–228 (2018).
- H. Gao, B. Ji, I. Jäger, E. Arzt, P. Fratzl, *Proc. Natl. Acad. Sci. U.S.A.* **100**, 5597–5600 (2003).
- A. Heyde, L. Guo, C. Jost, G. Theralaulz, L. Mahadevan, *Proc. Natl. Acad. Sci. U.S.A.* **118**, e2006985118 (2021).
- A. M. Torres et al., *Proc. Natl. Acad. Sci. U.S.A.* **116**, 24457–24462 (2019).
- D. S. Wiersma, *Nat. Photonics* **7**, 188–196 (2013).
- Z. Liu, Y. Huang, *Protein Sci.* **23**, 539–550 (2014).
- S. Kumar, S. Tan, L. Zheng, D. M. Kochmann, *npj Comput Mater.* **6**, 73 (2020).
- D. R. Reid et al., *Proc. Natl. Acad. Sci. U.S.A.* **115**, E1384–E1390 (2018).
- M. J. Mirzaali, H. Pahlavani, A. A. Zadpoor, *Appl. Phys. Lett.* **115**, 021901 (2019).
- Y. Zhang, M.-T. Hsieh, L. Valdevit, *Compos. Struct.* **263**, 113693 (2021).
- F. V. Senhora, E. D. Sanders, G. H. Paulino, *Adv. Mater.* **34**, e2109304 (2022).
- M. Gumin, *WaveFunctionCollapse* (2021); <https://github.com/mxgrmn/WaveFunctionCollapse>.
- Materials and methods are available as Supplementary Materials.
- X. Yin, W. Chen, A. To, C. McVeigh, W. K. Liu, *Comput. Methods Appl. Mech. Eng.* **197**, 3516–3529 (2008).
- C. Coulaud, E. Teomy, K. de Reus, Y. Shokef, M. van Hecke, *Nature* **535**, 529–532 (2016).
- L. Wang et al., *Proc. Natl. Acad. Sci. U.S.A.* **119**, e2122185119 (2022).

## ACKNOWLEDGMENTS

This paper is dedicated to the memory of Prof. John H. Conway (1937–2020) for his “Game of Life,” which inspired this research. We acknowledge M. Gumin for helpful discussions and generously sharing his 3D *WaveFunctionCollapse* demo codes. We also thank M. Deagen for creating online interactive plots that demonstrate the 3D database and E. Sanders for helping to plot the elastic surfaces.

**Funding:** US National Science Foundation grant 1835735 (CSSI); Caltech Carver Mead New Adventures Fund; Caltech SURF program; and Peking University College of Engineering. **Author**

**contributions:** Conceptualization: K.L. and C.D.; Methodology: K.L.; Investigation: K.L. and R.S.; Visualization: K.L.; Funding acquisition: C.D. and K.L.; Project administration: C.D.; Supervision: C.D.; Writing—original draft: K.L.; Writing—review and editing: K.L., C.D., and R.S.

**Competing interests:** The authors declare that they have no competing interests. **Data and materials availability:** All data are available in the main text or the supplementary materials. **License information:** Copyright © 2022 the authors; some rights reserved; exclusive licensee American Association for the Advancement of Science. No claim to original US government works. <https://www.science.org/about/science-licenses-journal-article-reuse>

## SUPPLEMENTARY MATERIALS

[science.org/doi/10.1126/science.abn1459](https://science.org/doi/10.1126/science.abn1459)

Materials and Methods

Supplementary Text

Figs. S1 to S9

Movies S1 to S3

Submitted 8 November 2021; accepted 20 July 2022  
10.1126/science.abn1459

## Growth rules for irregular architected materials with programmable properties

Ke LiuRachel SunChiara Daraio

Science, 377 (6609), • DOI: 10.1126/science.abn1459

### An irregular plan

Materials with irregular microstructures are common in the natural world and often have interesting properties. Liu *et al.* devised a growth-inspired program for generating irregular materials from a limited number of basic elements. Using building blocks with arbitrary complexity, the authors stochastically connected them subject to a set of local rules. The results echoed the diversity of natural systems with a large range of functional properties. —BG

### View the article online

<https://www.science.org/doi/10.1126/science.abn1459>

### Permissions

<https://www.science.org/help/reprints-and-permissions>



## Supplementary Materials for

### **Growth rules for irregular architected materials with programmable properties**

Ke Liu, Rachel Sun, Chiara Daraio

Corresponding author: Chiara Daraio, [daraio@caltech.edu](mailto:daraio@caltech.edu).

*Science* **377**, 975 (2022)  
DOI: 10.1126/science.abn1459

#### **The PDF file includes:**

Materials and Methods  
Supplementary Text  
Figs. S1 to S9

#### **Other Supplementary Material for this manuscript includes the following:**

Movies S1 to S3

## Materials and Methods

### Sample fabrication

The physical samples are 3D printed using the NinjaTek Semiflex filament (Fenner Inc.) on CraftBot Plus FFF 3D printers. Each sample is of size 100mm×100mm×15mm. We measured the linear elastic properties of the Semiflex material, and obtained its Young's modulus as  $E_S = 52.53$  MPa, and Poisson's ratio as  $\nu_S = 0.46$ . The 3D model is printed by the Sintratec Kit SLS printer (Sintratec AG) using Nylon material.

### FEM simulations

The mechanical properties of the 2D SVE samples are evaluated using custom homogenization code written in Matlab, based on square-shaped Q4 elements, using periodic boundary condition, assuming plane stress. Direct simulation on the 40×40 samples are performed without periodic boundary condition. Each building block is mapped to a 20×20 pixelated discretization. The solid parts are modeled as linear elastic material with properties of the Semiflex material. The voids are modeled as a very soft material ( $E_V = 0.001E_S$ ,  $\nu_V = 0$ ), a technique that is often used in the field of topology optimization. The examples in fig. 5 are performed in Comsol using second order triangular elements.

The mechanical properties of the 3D samples are evaluated using custom homogenization code written in Matlab, based on frame elements, with 3 translational and 3 rotational degrees of freedom at each node, using periodic boundary condition.

From the homogenization analyses, we obtain the material's effective elasticity tensor  $C$ , which describes the material's infinitesimal response in all directions. The commonly used material properties, such as the Young's modulus and Poisson's ratio, are functions of the elasticity tensor. Let  $S = C^{-1}$  as the compliance tensor, the inverse of  $C$ . Denote  $\sigma$  and  $\epsilon$  as the stress and strain tensor, respectively. If we define  $E_x$ ,  $E_y$ , and  $E_z$  as the Young's moduli in the  $x$ ,  $y$ , and  $z$  directions, respectively, they are given by:

$$E_x = \frac{\sigma_{11}}{\epsilon_{11}} = \frac{1}{S_{1111}}, E_y = \frac{\sigma_{22}}{\epsilon_{22}} = \frac{1}{S_{2222}}, E_z = \frac{\sigma_{33}}{\epsilon_{33}} = \frac{1}{S_{3333}}. \quad (1)$$

The average Young's modulus used in this article is defined as the average of the Young's moduli in different directions. For 2D:

$$E_{avg} = \frac{1}{2}(E_x + E_y). \quad (2)$$

For 3D:

$$E_{avg} = \frac{1}{3}(E_x + E_y + E_z). \quad (3)$$

Similarly, the Poisson's ratio along different directions are defined by:

$$\begin{aligned} \nu_{xy} &= -\frac{\varepsilon_{21}}{\varepsilon_{11}} = -\frac{S_{2211}}{S_{1111}}, \nu_{yx} = -\frac{\varepsilon_{12}}{\varepsilon_{22}} = -\frac{S_{1122}}{S_{2222}}, \\ \nu_{yz} &= -\frac{\varepsilon_{32}}{\varepsilon_{22}} = -\frac{S_{3322}}{S_{2222}}, \nu_{zy} = -\frac{\varepsilon_{23}}{\varepsilon_{33}} = -\frac{S_{2233}}{S_{3333}}, \\ \nu_{xz} &= -\frac{\varepsilon_{31}}{\varepsilon_{11}} = -\frac{S_{3311}}{S_{1111}}, \nu_{zx} = -\frac{\varepsilon_{13}}{\varepsilon_{33}} = -\frac{S_{1133}}{S_{3333}}. \end{aligned} \quad (4)$$

The average Poisson's ratio used in this article is defined as the average of the Poisson's ratio in all relevant directions. For 2D:

$$\nu_{avg} = \frac{1}{2}(\nu_{xy} + \nu_{yx}). \quad (5)$$

For 3D:

$$\nu_{avg} = \frac{1}{6}(\nu_{xy} + \nu_{yx} + \nu_{yz} + \nu_{zy} + \nu_{xz} + \nu_{zx}). \quad (6)$$

The shear modulus of a 2D material is obtained by:

$$G = \frac{1}{S_{1212}}. \quad (7)$$

For 3D, we can define shear moduli for different directions as:

$$G_{xy} = \frac{1}{S_{1212}}, G_{yz} = \frac{1}{S_{2323}}, G_{xz} = \frac{1}{S_{1313}}. \quad (8)$$

### Mechanical testing and DIC

The physical samples are tested on a Instron E3000 universal testing station with a 500-N load cell. The experimental setup is shown in fig. S3 and movie S2. The samples are placed in between two custom made aluminum fixtures. The contact surfaces between the fixtures and the samples are lubricated by silicone lubricant with Teflon (DuPont, Inc.), to reduce friction. For

the constituent material (Semiflex), tensile tests are conducted on five dog-bone samples (ASTM D638 Type IV). The Digital Image Correlation (DIC) analysis uses the VIC-2D system by Correlated Solution, Inc. The speckled patterns are sprayed onto the samples using an air brush. The DIC software captures the structures as point clouds and records the displacement of each point. A rectangular bounding box is defined by averaging the locations of points within a 10 mm strip, next to each side of the bounding box. The deformation of the bounding box in each direction is used to compute the average strains of the material sample. The average strains in the axial and lateral directions are then used to calculate the experimental Poisson's ratio, for axial strain approximately within the range of 0.005-0.015.

### The virtual growth program

The virtual growth program is written in C#, modified from the “Wave Function Collapse” code published by Maxim Gumin (@mxgmn) on GitHub. Our modified version (2D) is also uploaded to GitHub, which is accessible from: [https://github.com/Daraio-lab/Virtual\\_Growth\\_Program](https://github.com/Daraio-lab/Virtual_Growth_Program). The resultant databases (fig. 4) can be accessed from the same link. Details of the algorithm is presented in the Supplementary Text. The 3D version and corresponding data is available upon request to the corresponding author.

## Supplementary Text

### The virtual growth program

The implemented version of virtual growth program in the current research consists of three main input elements, which serve as the fundamental blueprint for the generation of the architected materials: (i) the basic building blocks, (ii) the adjacency rules, and (iii) the frequency hints, or target probabilities, of the basic building blocks.

The basic building blocks are elemental geometries that can be combined to produce complex structures, for example, the four basic building blocks shown in fig. S1B (“T”-shape, “L”-shape, “-”-shape, and “+”-shape). In 2D, each basic building block also has eight orientations through reflections and rotations, but some of them are identical due to symmetry. As shown in fig. S1B, there are four distinct orientations for the “T”-shaped building block, four for the “L”-shaped building block, two for the “-”-shaped building block, and only one for the “+”-shaped building block. The adjacency rules define whether and how the basic building blocks can pair with each other spatially, as illustrated in fig. 1C. The frequency hints of the basic building blocks influence how many times each building block would appear in the final design, which probabilistically controls the topology of the final design.

The growth process happens on a squared network of nodes for tile placement (fig. 1D). Starting from an initially random tile placement, the algorithm assigns to each node on the grid a random basic building block, but adjacency rules must be satisfied locally. In each step, the algorithm first finds the node with minimal nodal entropy. The nodal entropy  $S_i$  of node  $i$  is defined by

$$S_i = \sum_{j \in \Omega_i} -P_j \log P_j. \quad (\text{S1})$$

In Equation (S1),  $\Omega_i$  refers to the set of building blocks that are admissible to node  $i$ . When one or more neighbors of node  $i$  have already been assigned, the number of available building blocks reduces due to the compatibility constraint imposed by the adjacency rules. The symbol  $P_j$  denotes the normalized probability of building block  $j \in \Omega_i$  to be chosen, such that  $\sum_j P_j = 1$ . In cases when multiple nodes have the same entropy, the algorithm randomly chooses one of them. This applies also to the initialization step when all nodes are empty, and at the highest nodal entropy. After a node is chosen, the algorithm assigns a random building block

to it, sampled from all admissible ones according to their probabilities. Next, the algorithm updates the admissible sets and nodal entropy values of all remaining empty nodes, and repeats this procedure until all nodes are assigned. This process is illustrated in fig. S1D and movie S1. Defects can form when the admissible set of building blocks for a node becomes empty. This happens when the algorithm cannot assign any building block that it is simultaneously compatible with all neighboring nodes already assigned, according to the adjacency rules. Because the microstructures are composed of predefined building blocks and constructed following rules that guarantee local compatibility, the final designs have no disconnected parts, with boundaries and interfaces precisely defined.

The minimal nodal entropy heuristic ensures that the system’s total entropy decays at the lowest rate, and thus results in a smaller chance of defects. The node with minimal entropy in each step of “growth” is most likely to be a neighbor of the last assigned node, because the assignment of one node reduces the number of admissible building blocks in its neighboring nodes.

Although the virtual growth program is most suitable to produce irregular microstructures, it can also generate periodic ones. When the adjacency rules apply to opposite boundaries of a finite grid, we obtain microstructure motifs that can be periodically tessellated. This is equivalent as if the opposite boundaries of a finite grid become connected to each other, topologically forming a torus.

The frequency hints used to construct the databases in fig. 4 and 6 of the main text are generated by the following procedure. Denoting the frequency hint of each building block as  $w_i$ , to have a relatively complete coverage of all possible combinations of frequency hints, we need to uniformly sample the space of  $\{w_i\}$  constrained by  $\sum_i w_i = 1.0$ . The sampling algorithm follows the symmetric Dirichlet distribution, with screening to ensure relatively evenly spaced points, which leads to 180 different combinations of frequency hints. To uniformly sample points on the hyperplane of  $\sum_i w_i = 1.0$ , we first draw  $n$  reals  $(p_1, p_2, \dots, p_n)$  on the interval  $(0,1)$ , following a uniform distribution. Then we define intermediate variables  $q_i = -\log p_i$ . Finally, we let  $w_i = q_i / \sum_i q_i$ , so that  $w$  has a symmetric Dirichlet distribution, which is equivalent to a uniform distribution over the open standard  $(n - 1)$  simplex. After a new point is sampled, its Euclidean distances to all existing points are calculated, and only when all distances are larger

than a prescribed value  $d$ , this new point is accepted. This procedure leads to uniformly distributed points on the hyperplane of  $\sum_i w_i = 1.0$ , with density controlled by the parameter  $d$ .

### Expansion of Property Space

In plane elasticity, materials' elastic properties are categorized into four different symmetry classes: isotropic, tetragonal, orthotropic, and fully anisotropic. These symmetry classes characterize how a material responds to deformations in different spatial directions. For an architected material with periodic microstructure, its material symmetries are directly related to the geometric symmetry of its periodic unit cell. For example, a square-shaped unit cell with a four-fold symmetric pattern tessellates into a material whose elastic property is of tetragonal symmetry. A tetragonal material behaves the same in the  $x$  and  $y$  directions, but not in all directions. In examples shown in figs. 3 & 4 of the main text, although the microstructures generated by the virtual growth program are irregular, their ensembles, i.e., the bulk materials, exhibit elastic responses that are close to the tetragonal symmetry. This is due to both the choice of a squared grid and the limited selection and orientation of building block geometry. To demonstrate the ability to control and expand material symmetries, we demonstrate two possible approaches: (i) fine-tuning the building block frequencies for different orientations, and (ii) introducing new block geometries.

In all examples shown in figs. 3 & 4 of the main text, each possible orientation of a building block was treated to have equal probability of occurrence. Therefore, the resultant microstructure showed no directional preference over the  $x$  and  $y$  directions, which is the reason why the materials display tetragonal symmetry. To expand the achievable material properties' space, we now assign unequal frequency hints to different orientations of the building blocks, as illustrated in fig. S6. We separate the “T”-shaped and “—”-shaped building blocks into two groups: one with major load path along the  $x$  direction, and the other with major load path along the  $y$  direction. We gradually change the relative probability of the two groups from 50%-50% to 90%-10% (fig. S6A). For each of the new frequency hints, the resultant material properties are evaluated from 100 samples as before. Two representative samples are shown in fig. S6B. This change of frequency hints tunes the material elastic properties from tetragonal to orthogonal symmetry. As we increase the relative probability of the  $x$ -major group, the Young's modulus of the generated material increases in  $x$  direction, but decreases in  $y$  direction (fig. S6C). The

Poisson's ratio also changes along different directions. As the relative probability of the  $x$ -major group increases,  $\nu_{yx}$  becomes more negative, while  $\nu_{xy}$  becomes less negative (fig. S6D). We also observe that the distribution of  $\nu_{yx}$  over 100 samples become wider, while the distribution of  $\nu_{xy}$  becomes narrower. Meanwhile, this change of frequency hints reduces the shear modulus ( $G$ ) of the material in all directions (fig. S6C), without inducing directional preference.

Using the four basic building blocks in fig. 1B leads to very weak directional Young's modulus in the  $45^\circ$  directions (fig. S6C). To improve the Young's modulus in these directions, we introduce three new basic building blocks: the “O”-shape, the “V”-shape, and the “\”-shape (fig. S6E). We generate a new set of architected materials generated using all seven basic building blocks and compare their properties to architected materials generated only using the four initial blocks. Each set has 100 samples generated using the same inputs. The two sets are chosen such that they exhibit similar Young's modulus in the  $x$  direction. Two representative samples from each set are shown in fig. S6F. We observe that adding more “O”-shaped building blocks significantly improves the Young's modulus in the  $45^\circ$  directions, without sacrificing the Young's modulus in the  $x$  and  $y$  directions (fig. S6G). In addition, the new set of materials displays a more isotropic shear modulus compared to materials obtained from only four building block types. The presence of “O”-shaped building blocks plays an important role in increasing the Poisson's ratio, pushing both  $\nu_{xy}$  and  $\nu_{yx}$  from around 0.05 to around 0.65 (fig. S6H).

### Visualization

For the 3D irregular architected materials, we have created online interactive plots to present the data: <https://observablehq.com/@mdeagen/cg09>, thanks to the help from Dr. Mike Deagen ([mike.deagen@gmail.com](mailto:mike.deagen@gmail.com)).

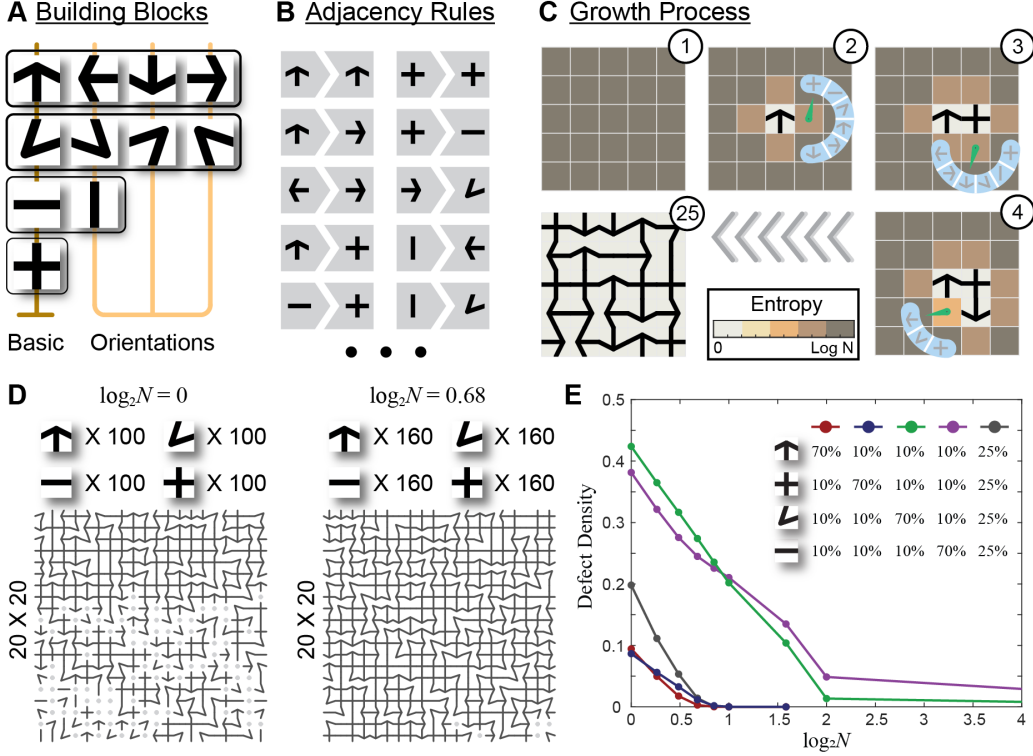


**Fig. S1.**

(A-C) Illustration of the “virtual growth” process in 2D on a  $5 \times 5$  grid of nodes. (A) Four basic building blocks (“T”-shape, “L”-shape, “-”-shape, and “+”-shape) and their possible orientations for the “virtual growth” of materials. (B) Examples of local adjacency rules. Each rule specifies how two basic building blocks connect to each other. (C) At each step, the node with minimal entropy is randomly assigned with one of the building blocks from (A), according to the frequency hints. This building block must be compatible with its neighbors, specified by the adjacency rules in (B). (D-E) Emergence of defects on  $20 \times 20$  grid of nodes. The parameter  $N$  denotes the ratio of the number of available building blocks over total number of nodes. (D) Typical defected designs for different  $N$ . The gray dots indicate defects, where no available building block can be assigned while satisfying compatibility constraints. When  $N = 1$ , all available building blocks must be perfectly fitted into all nodes, which is typically not possible and thus leaves many defects. (E) For each combination of initial frequency hints, 1000 samples of  $20 \times 20$  grid of nodes are generated and counted. The density is defined as the ratio of nodes with no compatible building block to assign over all available nodes (i.e., 400). Different colors refer to different combinations of initial frequency hints, as shown by the inset. When  $N = \infty$ ,

the frequency hints do not change due to assignment of building blocks, which reflects all examples in the main text of this paper. When  $N$  is finite, the assignment of a certain building block type onto a node reduces its frequency hint. When there are more “—” and “L”-shaped building blocks than “+” and “T”-shaped building blocks in the environment, defects are more likely to occur. This is because the “—” and “L”-shaped basic building blocks have less degrees (or local connectivity).

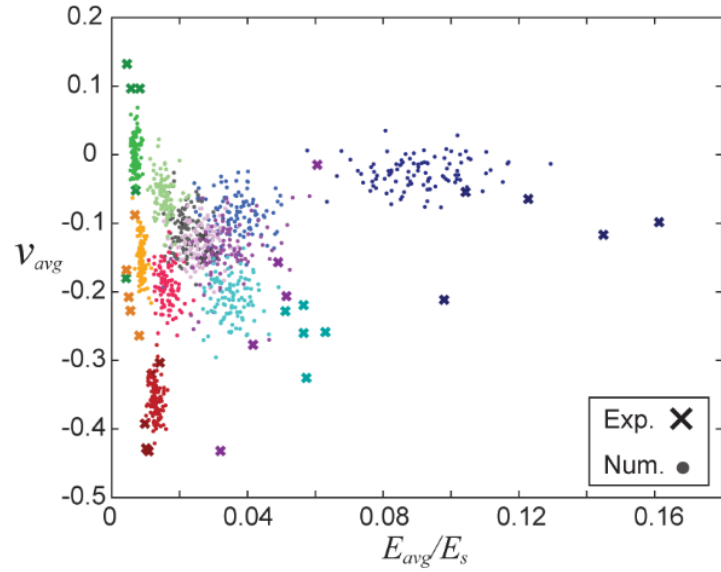


**Fig. S2.**

Clusters of numerical and experimental data. Each data point refers to an independent sample. Color code follows Fig. 3B in the main text. The values of  $E_{avg}$  and  $v_{avg}$  are taken as the average of measured values in  $x$  and  $y$  directions.

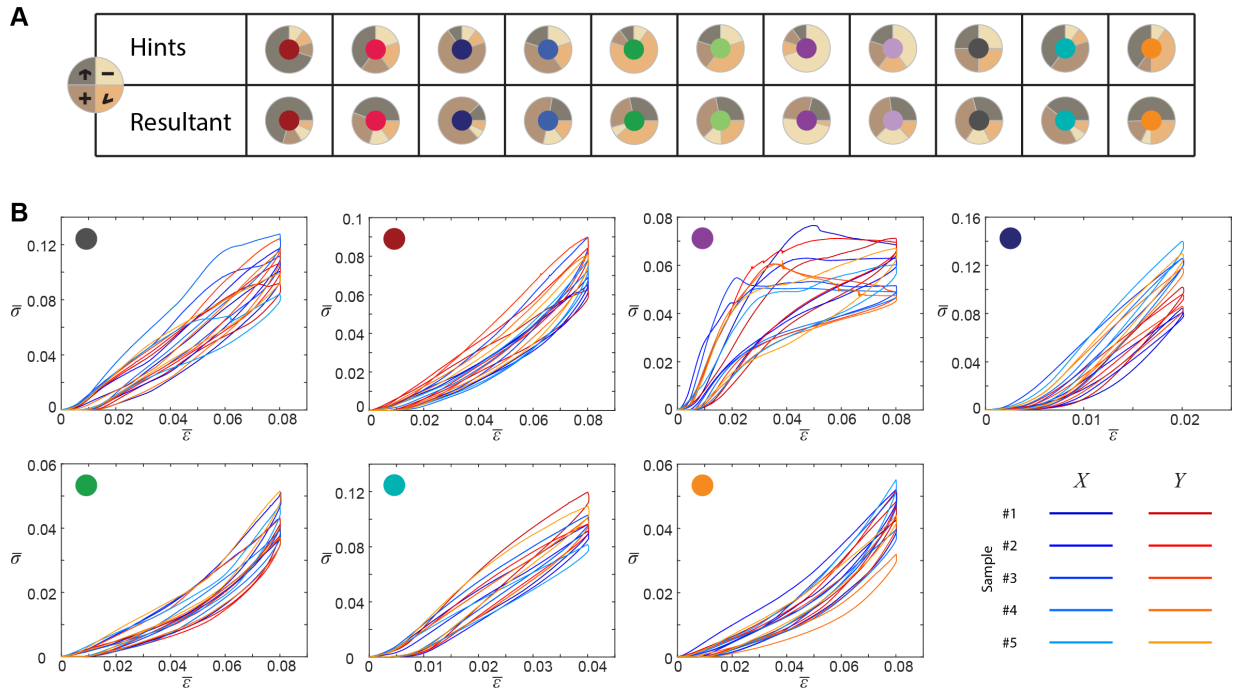


**Fig. S3.**

Additional information from the experiments. (A) Differences between the prescribed frequency hints and resultant probabilities of appearance. (B) All stress-strain curves of the 7 groups, each containing 5 samples loaded in both  $x$  and  $y$  directions. The colored dots in the graphs correspond to different frequency hints as shown in (A).

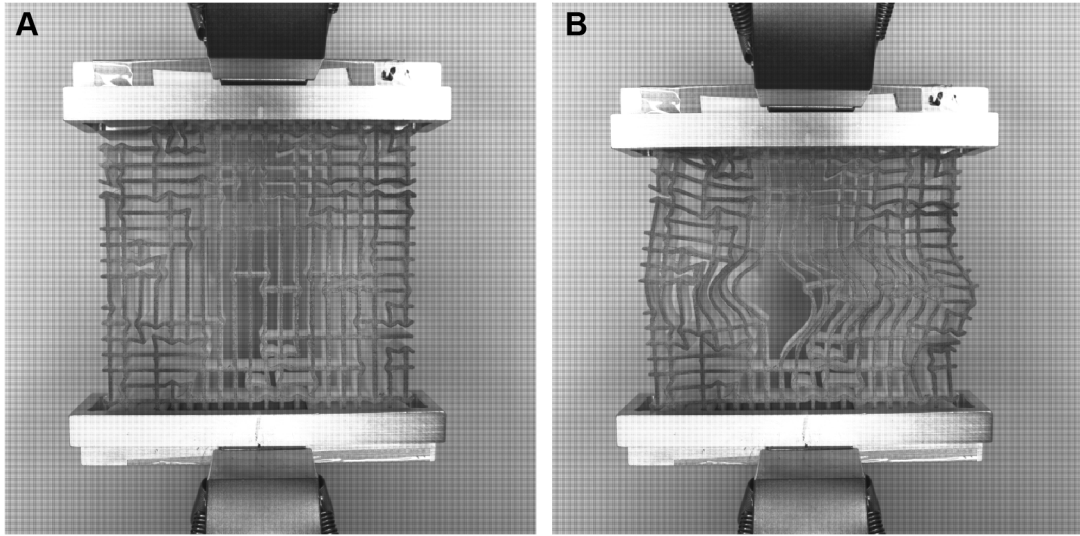


**Fig. S4.**

Snapshots from the experiment. (A) A sample of random architected material (from the same group shown in fig. 3G of the main text) before loading. The sample is placed in between two custom made aluminum blocks with shaped slots. (B) The deformed shape of the sample at 0.08 global (compressive) strain. Strong local nonlinear behavior is observed, resulting in contacts between buckled elements and friction.

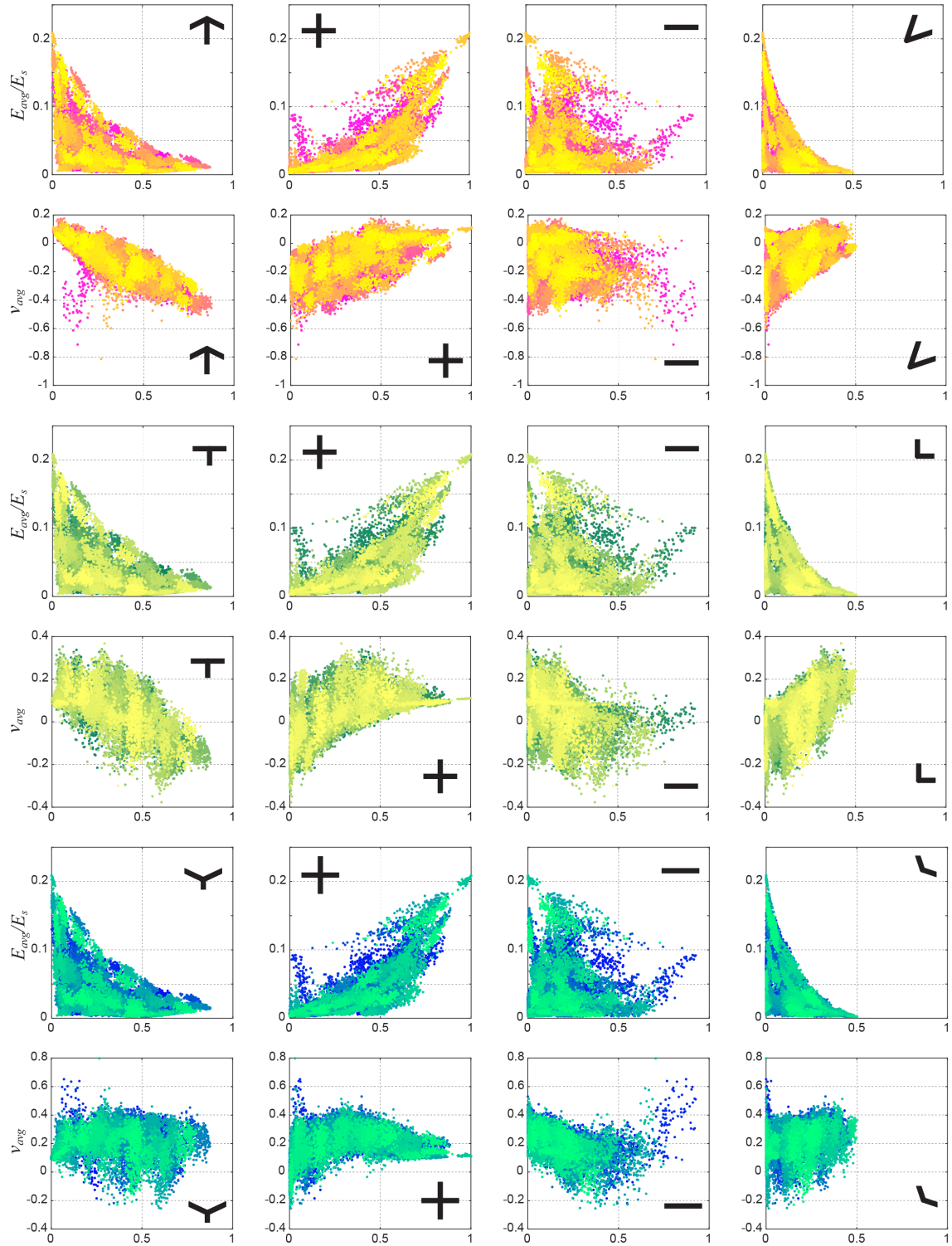


**Fig. S5.**

Influence of the probability of appearance of the basic building blocks on different mechanical properties. The horizontal axis of each diagram is the probability of appearance of the building

block shown as inset within the diagram. Each color contains 100 samples generated using the same growth rules.

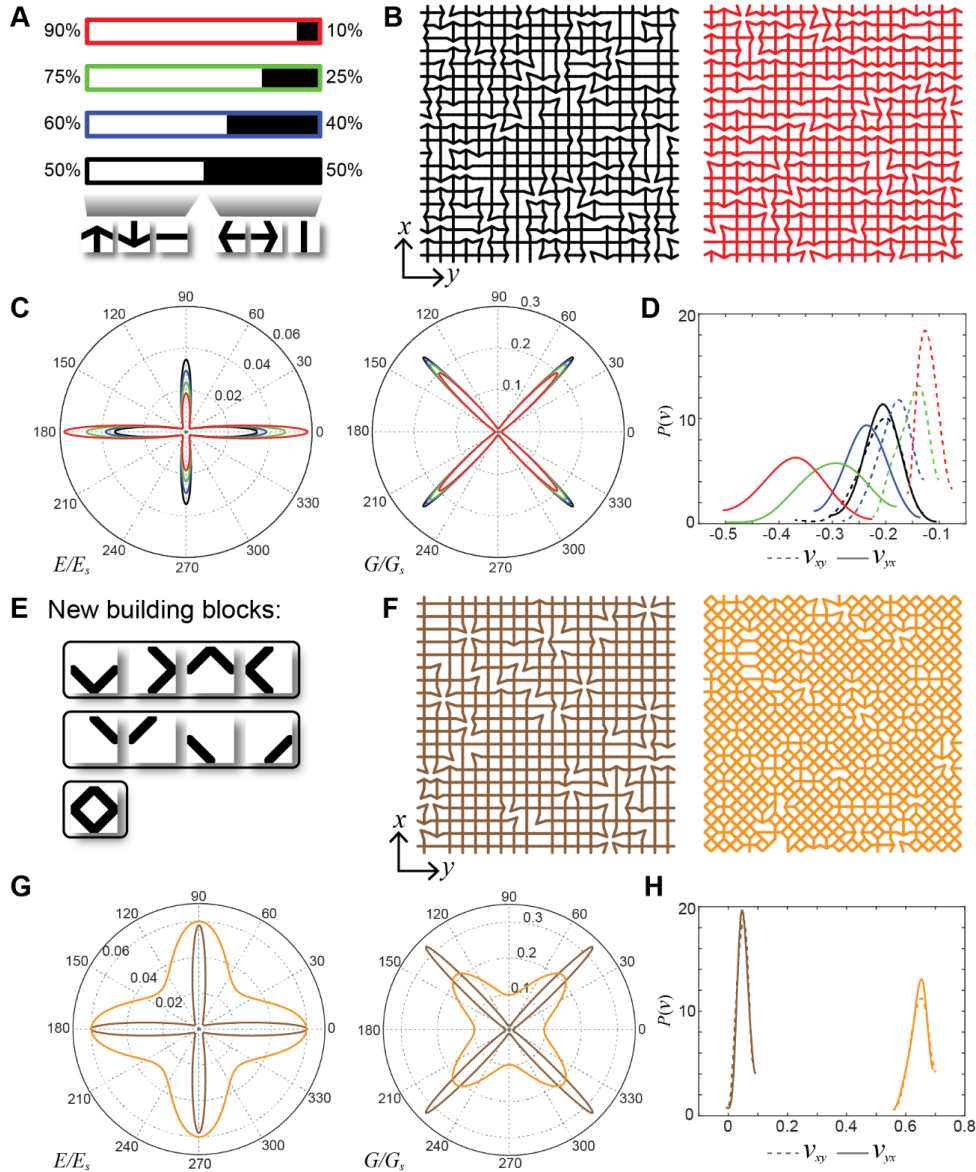


**Fig. S6.**

Expansion of property space by altering inputs to the virtual growth program. (A) Change of frequency hints of the “T” and “-” building blocks in different orientations. The baseline frequency hints are: 40% “T”, 40% “+”, 10% “-”, 10% “L”. (B) Representative designs generated by biased frequency hints. The left and right correspond to the 50%-50% and 90%-10% groups, respectively. (C) Directional mechanical responses, normalized Young’s modulus ( $E/E_S$ ) and normalized Shear modulus ( $G/G_S$ ) of the four groups in (A), each averaged over 100 samples.  $G_S$  denotes the shear modulus of the constituent material. (D) Distribution of

directional Poisson's ratios ( $\nu_{yx}$  and  $\nu_{xy}$ ) of the four groups in (A). (E) Three additional basic building blocks and their possible orientations. They are referred to as the “V”-shape, “\”-shape, and “O”-shape, from top to bottom. (F) Representative designs from two groups of samples, generated without (brown) and with (orange) the new building blocks, from left to right. The frequency hints of the group with 4 basic building blocks: 3.03% “T”, 66.01% “+”, 8.57% “-”, 22.39% “L”. The frequency hints of the group with 7 basic building blocks: 4.73% “T”, 15.53% “+”, 2.66% “-”, 6.29% “L”, 66.01% “O”, 1.26% “V”, 3.52% “\”. (G) Directional mechanical responses of the two groups. (H) Distribution of directional Poisson's ratios ( $\nu_{yx}$  and  $\nu_{xy}$ ) of the two groups in (E).

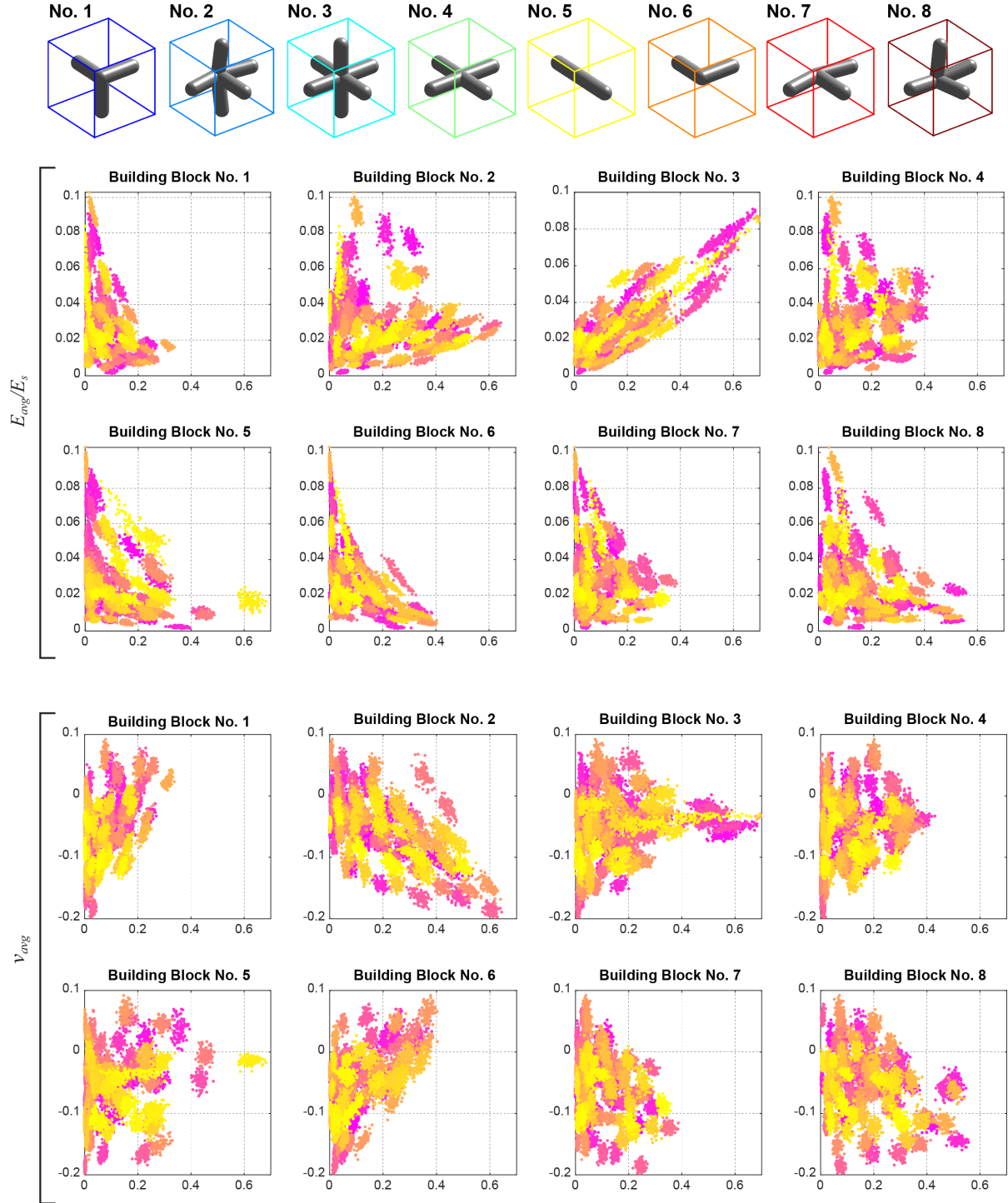


**Fig. S7.**

Influence of the probability of appearance of the basic building blocks on different mechanical properties for database #1 in fig. 6 of the main text. The horizontal axis of each diagram is the

probability of appearance of the corresponding building block. Each color contains 100 samples generated using the same growth rules.

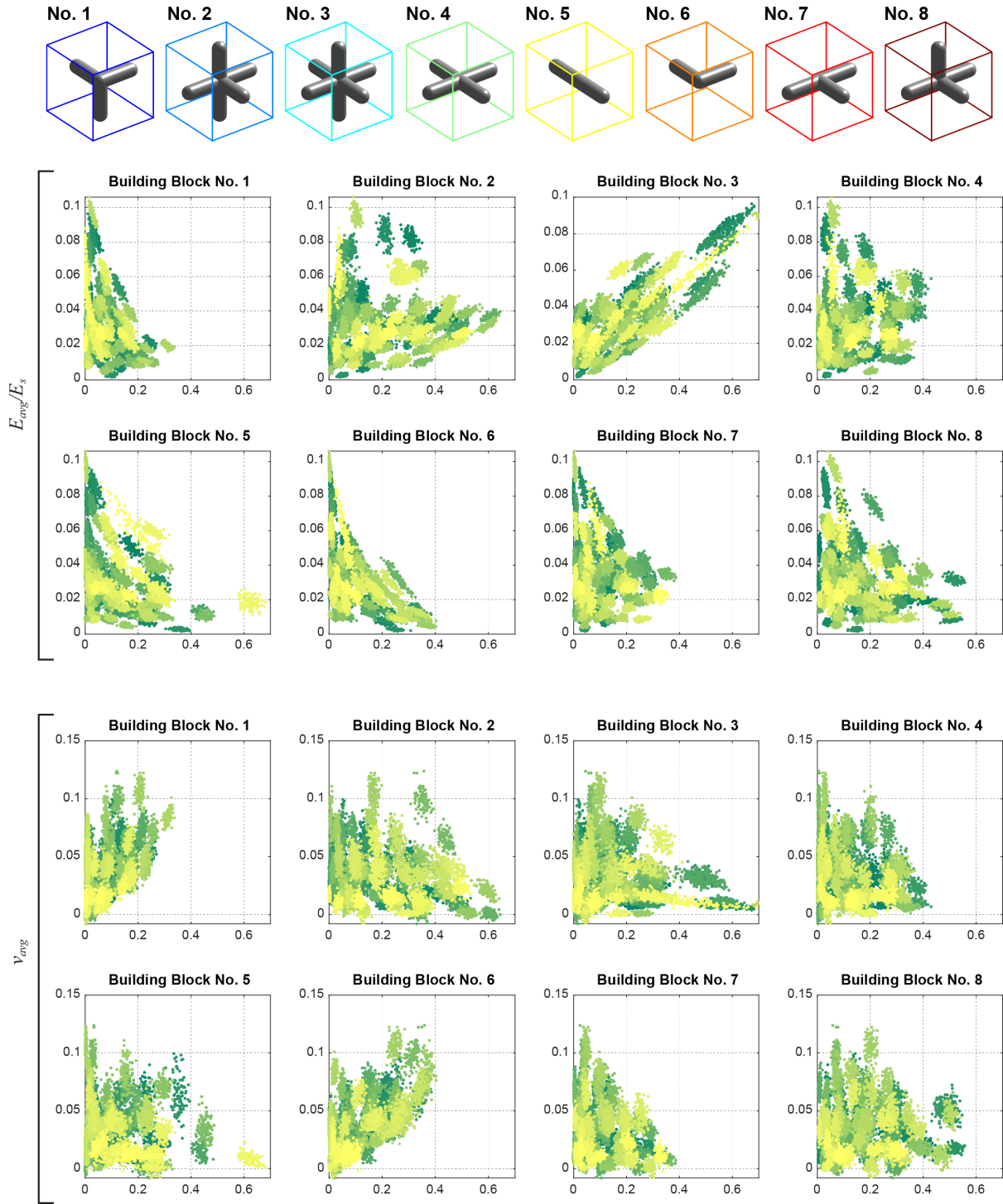


**Fig. S8.**

Influence of the probability of appearance of the basic building blocks on different mechanical properties for database #2 in fig. 6 of the main text. The horizontal axis of each diagram is the

probability of appearance of the corresponding building block. Each color contains 100 samples generated using the same growth rules.

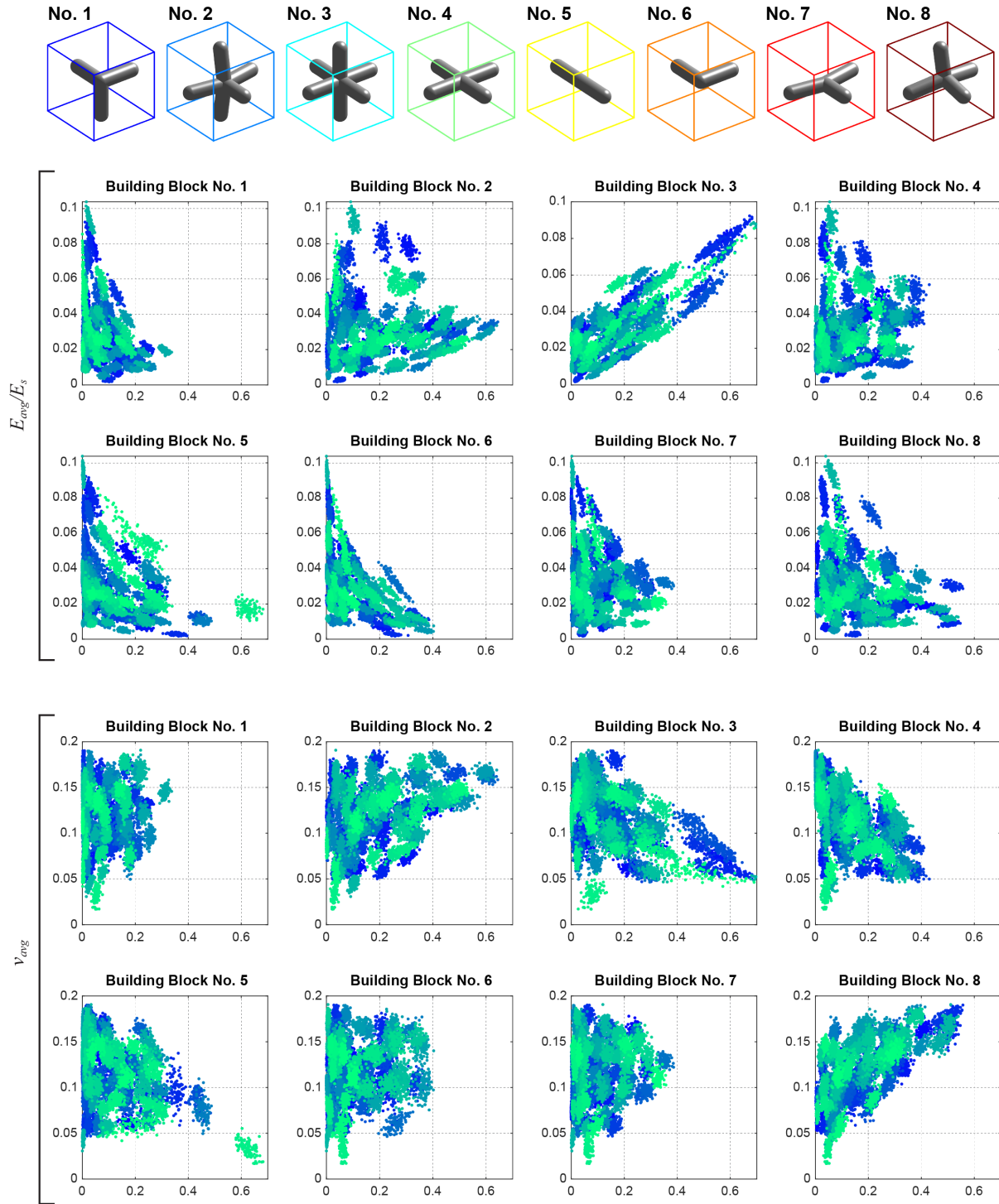


**Fig. S9.**

Influence of the probability of appearance of the basic building blocks on different mechanical properties for database #3 in fig. 6 of the main text. The horizontal axis of each diagram is the

probability of appearance of the corresponding building block. Each color contains 100 samples generated using the same growth rules.